Sustainable Energy & Fuels

ROYAL SOCIETY OF CHEMISTRY

REVIEW

View Article Online
View Journal | View Issue

Cite this: *Sustainable Energy Fuels*, 2025, **9**, 1432

Separator membranes for aqueous zinc–manganese oxide batteries: a comprehensive review on experimental results and theoretical simulations

T. Rodrigues-Marinho,[ab] D. Miranda,[bc] J. C. Barbosa,[d] R. Gonçalves,[d] S. Lanceros-Méndez *[aef] and C. M. Costa *[ag]

Lithium-ion batteries (LIBs) present the highest gravimetric and volumetric energy density, among the different rechargeable battery systems on the market, but still present safety and environmental issues. Thus, batteries based on different chemistries are being explored. Zinc–manganese oxide batteries represent a promising approach since they use components that are more readily available and accessible, especially in light of the scarcity of resources such as lithium. This review focusses on separator materials and the corresponding interface layers for zinc–manganese oxide batteries, from theoretical and experimental points of view, providing an overview of the most recent studies and advancements in the field. The primary obstacles still limiting the widespread application of these batteries are also covered.

Received 26th December 2024
Accepted 30th January 2025

DOI: 10.1039/d4se01817f

rsc.li/sustainable-energy

1. Introduction

The growing interest in renewable energy generation systems, which need to be associated with convenient storage systems in order to achieve their full potential, has spurred the search for efficient alternatives to traditional lithium-ion battery (LIB) systems.[1] The widespread use of these systems, which are estimated to account for around 60% of the total operational electrochemical storage power capacity, particularly at the level of electric mobility, is raising concerns regarding the scarcity of critical materials for LIB manufacturing.[2] These materials include lithium, cobalt, and nickel, among others,[3] and demand for some of those materials is expected to exceed available reserves in the near future.[4] The overexploitation of these materials will create pressure on natural resources, which can lead to increased manufacturing costs, as well as environmental issues.[5] In this context, the search for effective alternatives is becoming critical to diversify the range of materials used in energy storage systems, reducing the pressure on each individual one.[1]

In this regard, the development of technologies such as zinc–manganese oxide batteries represents a promising alternative, as they use materials with higher availability and accessibility on earth than lithium, representing lower risks of overexploitation.[6] Also, these batteries are relatively simple to produce, which can contribute to reduced manufacturing costs. It is estimated that the cost of raw materials for this type of device ranges between 15 and 30 $ per kW h, a suitable value for energy storage application.[7] Furthermore, it has been predicted that with the right processing procedures and materials, these batteries can present performance and capacities comparable to those obtained in traditional LIB technologies, as the energy density of these batteries is 150 W h kg^{-1}, with an estimated capacity loss of 2% per year at room temperature.[2]

A typical zinc–manganese oxide battery is constituted of a Zn anode and a MnO_2 cathode, using a strong basic electrolyte such as potassium hydroxide.[2] Also, zinc metal-free anodes[8] and a Zn anode decorated with 3D porous-structured $Na_3V_2(PO_4)_3$ (ref. 9) have been used. They were first developed in 1952 and patented in 1960 by Marsal, Kordesch, and Urry.[10] This anode/cathode combination is advantageous due to the MnO_2 capacity to accommodate the Zn^{2+} cations, leading to a high theoretical capacity.[11] However, there are still several limitations for the wide application of this technology, such as the Zn dendrite growth, the occurrence of side reactions with the electrolyte solution and the collapse of the cathode structure.[6] In this regard, improved separator materials and theoretical

[a]*Physics Centre of Minho and Porto Universities (CF-UM-UP), Laboratory of Physics for Materials and Emergent Technologies, LapMET, University of Minho, 4710-057 Braga, Portugal. E-mail: cmscosta@fisica.uminho.pt*
[b]*2Ai – School of Technology, IPCA, Barcelos, Portugal*
[c]*LASI – Associate Laboratory of Intelligent Systems, Guimarães, Portugal*
[d]*Centre of Chemistry, University of Minho, Braga 4710-057, Portugal*
[e]*BCMaterials, Basque Center for Materials, Applications and Nanostructures, UPV/EHU Science Park, 48940, Leioa, Spain. E-mail: senentxu.lanceros@bcmaterials.net*
[f]*IKERBASQUE, Basque Foundation for Science, 48009, Bilbao, Spain*
[g]*Institute of Science and Innovation for Bio-Sustainability (IB-S), University of Minho, 4710-053 Braga, Portugal*

modeling of zinc–manganese batteries can support overcoming the present limitations. By the theoretical modelling of the materials, architecture and operation of the devices, the main issues affecting battery performance can be identified. This kind of simulation can be a complex topic, as all the components and mechanisms must be accurately described.[12] This work reviews the relevant issues and advances in theoretical simulations and separators for zinc–manganese oxide batteries, as materials for electrodes (Zn||MnO_2 (ref. 2, 6 and 13)) and aqueous electrolyte solutions[14] have recently been addressed.

2. Aqueous zinc–manganese oxide batteries

In the scope of energetic requirements for human daily activity, energy storage systems are required for the increased mobility and portability of devices and to optimize the use of intermittent renewable energy sources, such as wind and solar energy. At present, lithium-ion batteries (LIBs) and lead–acid batteries dominate the market[15] even with the use of toxic lead (lead–acid batteries), large volumetric occupation, environmental issues, and low energy densities (30–50 W h kg^{-1}) of the latter.[16] In the case of LIBs, the energy density is improved but the safety problems related to organic electrolytes still persist.[17] Environmentally friendly electrolytes with economic viability and high ionic conductivity can be obtained using aqueous secondary batteries.[18,19] Using batteries based on aqueous zinc ions (AZIBs) is a promising approach since the materials are of low cost and with low environmental impact fabrication.[20] A promising AZIB large-scale energy storage system is based on Zn/MnO_2 batteries since zinc presents a high theoretical capacity (820 mA h g^{-1}) with low redox potential (−0.76 V *versus* the hydrogen electrode),[21] low cost, and no toxicity, but with an anion radius larger when compared to the Li ion. Mn-based materials present a theoretical specific capacity of 308 mA h g^{-1} (for the one-electron redox reaction)[22] with non-toxicity and low cost production when compared to other oxide cathodes[22] and simple nanostructure production but with low electrical conductivity and instability.[23,24] The diversity of crystalline polymorphs in MnO_2 arises from the several ways the MnO_6 basic units are organized, being classified into three main types: layered structures (δ-MnO_2), tunnel structures (α-, β-, γ-, λ-, δ- and R-MnO_2) and stacked structures (ε-MnO_2). Consequently, the redox of MnO_2 can exhibit significant variation based on salt and pH values of the aqueous electrolyte.[22]

Batteries based on Zn/MnO_2 as primary cells are considered environmentally friendly and safe since they have been certified by the Environmental Protection Agency (EPA) for landfill disposal[25] and they are based on relatively abundant materials in the earth's crust.[26,27] For battery proposes, Zn/MnO_2 materials need to present reliability for long cycle lifetimes (higher than 4000 cycles) which means 10 to 15 years of battery life for energy storage applications.[28] The stability and energy density of aqueous Zn/MnO_2 batteries are nonetheless compromised by water splitting in aqueous electrolytes.[29,30] To enhance the cycling stability of the Zn/MnO_2 battery and reduce the water content, a quasi-solid electrolyte has been implemented by incorporating poly(vinyl alcohol) (PVA) into the aqueous electrolyte.[31]

At the cathode, the formation of manganite MnOOH occurs from a solid-state proton insertion mechanism from the reduction of MnO_2 due to the first electron discharge for voltages between 1.5 and 0.9 V.[32] For discharges lower than 0.9 V, the formation of manganese hydroxide ($Mn(OH)_2$) occurs due to a heterogeneous dissolution process from the reduction of MnOOH. The formation of other species such as $ZnMn_2O_4$ and Mn_3O_4 from the reduction of MnOOH at two-electron discharge (Table 1 and Fig. 1) was also observed by Gallaway and Menard.[33] The volume expansion of the Mn–O lattice from the reduction of MnO_2 leads to the formation of the irreversible, soluble and unstable Mn^{3+} species.[34] The solubilization of the Mn^{3+} species during the first and second electron discharge is related to the $ZnMn_2O_4$ and Mn_3O_4 formation.[35] To obtain a good cycling life of the electrochemical reactions at the cathode, the reduction of the solubilization of the Mn^{3+} is required by restricting the depth of discharge (DOD)[36,37] which leads to a reduction in battery capacity. Although the applications of this restriction by despite this restriction, the capacity failure still occurs due to the formation of $ZnMn_2O_4$ and Mn_3O_4 presenting and insulating and electrochemical irreversible behavior.[36,37] Rechargeable Zn/MnO_2 batteries demonstrate extended cycle life at reduced DOD between 10% and 20% of the first electron of MnO_2 allowing a higher energy density with a cost lower than 100 $ per kW h.[37] The increased energy density obtained at higher DOD triggered detrimental phase

Table 1 Nominal half reactions during discharge of a Zn/MnO_2 battery

	Nominal half reactions during discharge
Anode	$Zn + 4OH^- = Zn(OH)_4^{2-} + 2e^-$
Cathode	$MnO_2 + H_2O + e^- = MnOOH + OH^-$
	$MnOOH + H_2O + e^- = Mn(OH)_2 + OH^-$
Overall	$Zn + MnO_2 + 2H_2O + 2OH^- \rightarrow Zn(OH)_4^{2-} + Mn(OH)_2$

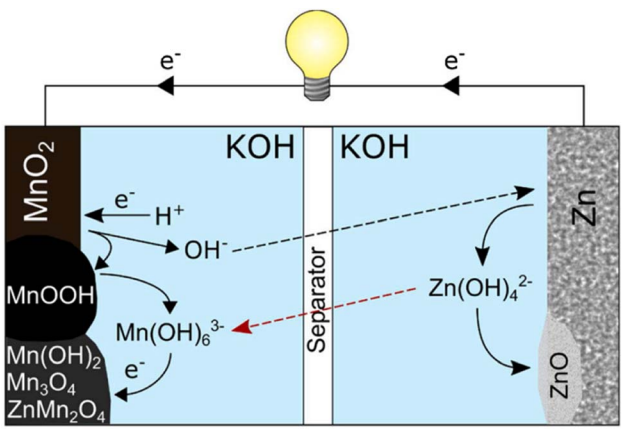

Fig. 1 Illustration of the discharge process of a Zn/MnO_2 battery with potassium hydroxide electrolyte. Reproduced from ref. 47, with permission. Copyright 2021, Elsevier.

transformation of MnO_2 (ref. 38) and zinc redistribution.[39,40] A nearly full two-electron capacity over 6000 cycles, even in the absence of zinc, is obtained using the birnessite type manganese dioxide (δ-MnO_2) and $Mn(OH)_2$ with copper and bismuth.[41]

During the second electron charge/discharge process, the zinc at the anode undergoes a reaction with OH^- to produce $Zn(OH)_4^{2-}$ which precipitates into ZnO.[39] The $Zn(OH)_4^{2-}$ species can be found across the entire cell even on the cathode due to the permeability of the separator layer, resulting in the deposition of an insulator layer of ZnO on the cathode or an irreversible reaction with Mn species to produce $ZnMn_2O_4$.[42,43] Over several cycles, the accumulation of the $ZnMn_2O_4$ species leads to a decrease of Mn atoms participating in the electrochemical reaction which continuously decreases the capacity and increases the cell resistance, diminishing the overall discharged energy and cell potential. Several studies were conducted to reduce the $Zn(OH)_4^{2-}$ concentration on the cathode side to prevent the Zn/MnO_2 battery failure using separators based on polymeric materials (presenting higher permeability to OH^- than to $Zn(OH)_4^{2-}$),[44] anionic exchange based on polystyrene separators,[45] and interlayers based on metal oxide materials to enhance the trapping of $Zn(OH)_4^{2-}$ species.[46] Table 1 summarizes the redox equations occurring at the cathode and anode and the overall reactions during the discharge process, as illustrated in Fig. 1.

The redox potential of Zn/MnO_2 batteries is dependent on the electrode composition and electrolyte concentration, producing an open circuit voltage between 1.4 and 1.7 V.[47] Despite the five decades of studies on Zn/MnO_2 batteries, the redistribution of the active material on the anode and the limitation of the rechargeable cycles, showing a lifetime between 20 and 30 cycles, are still the limiting factors.[47] The company Battery Technologies Inc. (BTI) developed Zn/MnO_2 batteries with a capacity retention lower than 50% after 25 cycles with a lifetime of 25 cycles,[48] which is poor compared with the rechargeability of LIBs.[47]

The main characteristics of different battery technologies based on AZIBs,[49] Zn/MnO_2,[50] LIBs[51,52] and sodium ion batteries (SIBs)[53,54] are summarized in Table 2 for comparison. The energy and power density have been estimated for AZIBs and Zn/MnO_2.

For Zn–MnO_2 batteries, the capacity and voltage are limited due to the one-electron redox reaction which can be theoretically increased to 570 mA h g^{-1} at the two-electron reaction of Mn^{4+}/Mn^{2+} species.[50] The performance of the batteries is diminished due to the instability and lower kinetics of the Zn ions being a drawback for large-scale production. The formation of zinc dendrites at high current, another limitation of these batteries, can be addressed with surface coating, mild acidic aqueous electrolytes or the substitution of the anode current collector.[55] The unregulated growth of dendrites poses a substantial risk to the integrity of the anode–electrolyte interface leading to the failure of battery performance. This effect is connected to the local distribution of the electric field, surface texture and the zincophilicity of the substrate.[56,57] Efforts have thus been focused on modifying the anode–electrolyte interface and performing electrolyte engineering to suppress dendrite formation using an artificial anode–electrolyte interface to guide the smooth deposition of Zn^{2+}.[58–60] Aqueous electrolytes with molecules[61,62] and inorganic salts[63,64] have also been studied to solve dendrite formation, also supported by theoretical simulations.

2.1. Theoretical model

As mentioned before, theoretical modelling is gaining relevance to predict the best conformations and conditions for optimizing battery performance.

A basic electrode configuration consists of a solid metal electrode in contact with an electrolyte. In this setup, the electrochemical reaction occurs solely on the surface of the electrode. However, practical batteries use porous electrodes, implying that active electrode materials are not just at the surface, with the porosity affording a substantial reaction region owing to the electrode's high surface area.[65,66] In the Newman model, it is assumed that both the anode and cathode electrodes, as well as the separator, show a porous structure. It is essential to highlight that the electrolyte, in its liquid phase, is distributed within both the electrodes and the separator.[65–67] A porous electrode with a random structure can be defined by its porosity, tortuosity, average surface area per unit volume, and the average conductivity of the solid matrix. The separator prevents electron flow, meaning that all current passing through it is ionic. Conversely, the current collector allows only electron flow, making all current at the collector electronic. However, the total current passing through both the separator and the current collector remains constant during operation.

Table 2 Main materials and characteristics of different battery technologies

Properties	AZIB	Zn/MnO_2	LIB	SIB
Anode	Zn	Zn	Graphite	Hard carbon
Cathode	Vanadium-based $MFe(CN)_6 \cdot nH_2O$	MnO_2	$LiCoO_2$	$NaCoO_2$
			$LiNi_{1-x}M_xO_2$	$NaNi_{1-x}M_xO_2$
	Co_3O_4		$LiNi_xMMn_yMCo_zMO_2$	$NaNi_xCo_yMMn_zMO_2$
Electrolyte	Inorganic	Inorganic	Organic	Organic
Voltage (V)	0.6–1.8	1.2–2.8	3–5	2.5–4
Theoretical capacity (mAh g^{-1})	65–400	100–600	80–200	80–180
Energy density (W h kg^{-1})	100–200	70–400	150–260	120–220
Power density (W kg^{-1})	10–20 000	100–10 000	150–2000	40–500
Cost (kW per $)	450	<70	<1530	16.8

Between the separator and the current collector, the conversion between ionic and electronic current occurs at the solid-electrolyte interphase due to the electrochemical reactions.

Chen and Cheh[68] advanced on the understanding of alkaline battery discharge behavior by introducing a secondary distribution reaction model. This model considers factors such as the concentration (KOH concentration is 7 M), porosity, and the transference number of species, particularly focusing on their effects on the cathode region. The discharge behavior of the anode was characterized using a simplified mixed-reaction model. The authors further enhanced the model by incorporating a dissolution–precipitation reaction mechanism to elucidate anode discharge behavior, with the assumption that zincate ions were solely present in the anode region.[69] The effects of zincate ion transport throughout the entire cell and the temperature variations during discharge were studied in ref. 70 concluding that the temperature effects on alkaline Zn–MnO_2 are negligible. The discharge behavior over submicroscopic, microscopic, and macroscopic levels was evaluated in ref. 71 to provide a more precise description of alkaline battery behavior. The relation between the overpotential and the current density, considering the electrochemical kinetic relationships (linear kinetics and Tafel kinetics), can be obtained (eqn (1)) using the Butler–Volmer equation as:

$$i = i_0\left(\exp\left(\frac{\alpha_a nF\eta}{RT}\right) - \exp\left(-\frac{\alpha_c nF\eta}{RT}\right)\right) \quad (1)$$

where i_0 is the exchange current density, i_1 and i_2 are the current densities of the solid phase and electrolyte, η is the overpotential (potential difference between ϕ_1 – the potential of the solid phase and ϕ_2 – the potential of the electrolyte), α_a and α_c are the anodic and cathodic transfer coefficients, R is the universal gas constant, F is the Faraday constant, z is the number of electrons in the electrochemical reaction and T is the temperature. A simplified expression (eqn (2)) can be obtained at low overpotential, so the linear kinetics can be written as:

$$i = i_0\frac{nF}{RT}\eta \quad (2)$$

Furthermore, for high overpotential regions, the Tafel kinetics can be used to simplify the Butler–Volmer equation (eqn (3) and (4)) as:

$$\eta \ll 0 \quad i = -i_0\exp\left(-\frac{\alpha_c nF\eta}{RT}\right) \quad (3)$$

$$\eta \gg 0 \quad i = i_0\exp\left(-\frac{\alpha_a nF\eta}{RT}\right) \quad (4)$$

It is further necessary to consider some assumptions to solve this model in one dimension such as during the discharge process the system is at a steady-state and the concentration effects on current density and potential are not considered, as summarized in Table 3. At the current collector and separator, the current is electronic and ionic respectively. It is also assumed that the solid potential and liquid potential are zero at the separator and current collector, respectively.

The principle of mass conservation within the control volume dictates that the accumulation of each species equals (*e.g.* cation K^+, anion OH^-, $Zn(OH)_4^{2-}$, and water and two salts, *i.e.*, KOH and $K_2Zn(OH)_4$) the sum of the net influx of that species into the control volume and the production of that species resulting from electrochemical or chemical reactions. The governing equation for the mass balance of each species (eqn (5)) can be written as

$$\frac{\partial(\varepsilon c_i)}{\partial t} = -\nabla\cdot N_i + R_i \quad (5)$$

where ε is the porosity of each electrode, c_i is the species concentration in pore solution, N_i is the surface ionic flux on the porous electrode and R_i is the production rate of each species by the electrochemical reaction. The parameter R_i can be obtained (eqn (6)) using Faraday's law as

$$R_i = aj_{in} = -\frac{s_i}{nF}ai_n = -\frac{s_i}{nF}j \quad (6)$$

where a is the specific electrode area per volume, j_{in} is the solid phase to solution pore wall flux, s_i is the stoichiometric coefficient of the electrochemical reaction, n is the number of electrons, i_n is normal current density at the pore wall interface and j is the transfer current density per unit volume. The diffusion process occurs due to concentration fluctuations within the battery, the migration being related to the movement of charged species in the presence of an electric field and the convection is due to the movement of charged species within the bulk electrolyte. The Nernst–Planck equation (eqn (7)) describes the

Table 3 Boundary conditions for the porous electrodes

Boundary conditions at porous electrodes	
Governing equation	Physical process
$\frac{di_1}{dx} + \frac{di_2}{dx} = 0, \quad x = L, \ i_1 = I$	Charge conservation
$\frac{di_2}{dx} = ai_0\frac{nF\eta}{RT}$ or $\frac{di_2}{dx} = -ai_0\exp\left(-\frac{\alpha_c nF\eta}{RT}\right), \quad x = 0, \ i_2 = I$	Rate of electrochemical reactions
$i_1 = -\sigma\frac{d\phi_1}{dx}, \quad x = 0, \ \phi_1 = 0$	Ohm's law in solids
$i_2 = -\kappa\frac{d\phi_2}{dx}, \quad x = L, \ i_2 = 0$	Ohm's law in liquids

movement of charged species based on these three phenomena as:

$$N_i = -\varepsilon D_a \nabla c_i + \frac{i_2 t_i'}{n_i F} + c_i v' \quad (7)$$

The first term in eqn (7) is related to the diffusion, with D_a being the electrolyte effective diffusion coefficient and ∇c_i being the concentration gradient of each species on the electrode. The migration phenomena are expressed in the second term $(i_2 t_i'/n_i F)$ with i_2 being the ionic current density and t_i' being the transference number (it was assumed constant at battery discharge). The term $c_i v'$ describes the convection, with c_i being related to the instantaneous concentration of the species. The concentration of binary electrolytes can be expressed (eqn (8)) as:

$$c_a = \frac{c_1}{v_1^a} = \frac{c_2}{v_2^a} \quad (8)$$

The mass balance in the electrolyte can be obtained (eqn (9)) by substituting eqn (6)–(8) into eqn (5) as

$$\frac{\partial(\varepsilon c_a)}{\partial t} + v' \cdot \nabla c_a + c_a \nabla \cdot v' = \nabla \cdot \left(\varepsilon^{1.5} D_{a,\infty} \nabla c_a\right) - \left(\frac{1 - t_2'}{F}\right) \nabla \cdot i_2 \quad (9)$$

where c_a is the electrolyte concentration, D_a ($D_a = D_{a,\infty}\varepsilon^{1.5}$) is the effective diffusion coefficient and $D_{a,\infty}$ is the bulk electrolyte diffusion coefficient. Therefore, since water is neutral and migration can be neglected, the mass balance can be expressed (eqn (10)) as:

$$\frac{\partial(\varepsilon c_0)}{\partial t} + \nabla \cdot \left(c_0 v'\right) = \nabla \cdot \left(\varepsilon^{1.5} D_{a,\infty} \nabla c_0\right) - \frac{s_0}{nF} j \quad (10)$$

The continuity equation in the battery can be obtained by multiplying the electrolyte molar volume (V_a^-) and water molar volume (V_0^-) by eqn (9) and (10), respectively (considering the thermodynamic relationship ($c_a V_a^- + c_0 V_0^- = 1$)) (eqn (11)) as:

$$\frac{\partial \varepsilon}{\partial t} + \nabla \cdot v' = \left[\frac{V_0^-}{F} + \left(t_2' - 1\right)\frac{V_a^-}{F}\right] \nabla \cdot i_2 \quad (11)$$

The current density is zero ($\nabla \cdot i_1 + \nabla \cdot i_2 = 0$) due to the conservation law considering that the conversion from ionic to electronic current occurs at the active material/electrolyte interface. The conduction in the solid phase and electrolyte is described as eqn (12) and (13) respectively.

$$i_1 = -\sigma \nabla \phi_1 \quad (12)$$

$$\nabla \phi_2 = -\frac{i_2}{\kappa} + \frac{2RT}{F}\left(1 - t_2' + \frac{c_a}{c_0}\right) \nabla \ln \alpha_a \quad (13)$$

The charge balance can be obtained from Gauss's theorem for an electrode surface area of $H \times W$ (eqn (14)) as:

$$i_1 + i_2 = \frac{I}{HW} \quad (14)$$

The potential of the electrolyte is related to the ionic current density and chemical potential. Therefore, the overpotential for a Zn/MnO_2 battery can be expressed (eqn (15)) as:

$$\frac{\partial \eta}{\partial x} = i_2\left(\frac{1}{\varepsilon^{1.5}\kappa_\infty} + \frac{1}{\sigma}\right) - \frac{I}{HW\sigma} + \frac{2RT}{F}\left(1 - t_2' + \frac{c_a}{c_0}\right)\frac{\partial a_a}{a_a \partial x} \quad (15)$$

The overall solid balance (eqn (16)) can be obtained from Faraday's law as:

$$\frac{\partial \varepsilon}{\partial t} = \left[\frac{V_\alpha^-}{F} - \frac{V_\gamma^-}{F}\right]\frac{\partial i_2}{\partial x} \quad (16)$$

where the partial molar volume of α-MnOOH and γ-MnOOH is V_α^- and V_γ^- respectively. Then mass balance is related to the change of the radius (MnO_2) (eqn (17)) as

$$\frac{\partial r_0^3}{\partial t} = \frac{-3}{4\pi NF}\left[V_\alpha^- - V_\gamma^-\right]\frac{\partial i_2}{\partial x} \quad (17)$$

Therefore, the Butler–Volmer equation for the electrochemical reaction rate (eqn (18)) is

$$\frac{\partial i_2}{\partial x} = \frac{\exp\left(\frac{a_a F \eta}{RT}\right) - \exp\left(-\frac{a_c F \eta}{RT}\right)}{\frac{1}{a i_0} + \frac{-\exp\left(-\frac{a_c F \eta}{RT}\right)}{(\nabla \cdot i_2)_{\lim}}} \quad (18)$$

where $(\nabla \cdot i_2)_{\lim}$ is the limited transfer current related to the limitation of the proton's transportation on the particle shell (MnO_2). Therefore, the governing equations for Zn/MnO_2 batteries (eqn (19) and (20)) can be expressed as

$$\frac{\partial(\varepsilon c_a)}{\partial t} + v' \cdot \frac{\partial c_a}{\partial x} + c_a \frac{\partial v'}{\partial x} = \nabla \cdot \left(1.5\varepsilon^{0.5} D_{a,\infty} \frac{\partial c_a}{\partial x}\frac{\partial \varepsilon}{\partial x} + \varepsilon^{1.5} D_{a,\infty} \frac{\partial^2 c_a}{\partial x^2}\right) - \left(\frac{1 - t_2'}{F}\right)\frac{\partial i_2}{\partial x} \quad (19)$$

$$\frac{\partial \varepsilon}{\partial t} + \frac{\partial v'}{\partial x} = \left[\frac{V_0^-}{F} + \left(t_2' - 1\right)\frac{V_a^-}{F}\right]\frac{\partial i_2}{\partial x} \quad (20)$$

The theoretical modeling of Zn/MnO_2 batteries must be complemented with experimental testing in order to validate the data obtained by the simulations. Thus, some of the most relevant studies in the field are described in the following section.

2.1.1. Theoretical simulation results. Electric field distribution simulations have been carried out by Zeng, Zhang[72] to evaluate the dendrite formation on Zn anodes after Zn nucleation on Zn/carbon cloth and Zn/carbon nanotube (CNT) anodes. The authors demonstrated (Fig. 2a and b) that the Zn/carbon cloth anode surface presented irregular electric field distribution driving more adsorption of Zn^{2+} leading to Zn deposition. Nevertheless, the Zn/CNT anode surface demonstrated a more uniform electric field distribution (Fig. 2b) due to the higher specific surface area of CN frameworks and small Zn

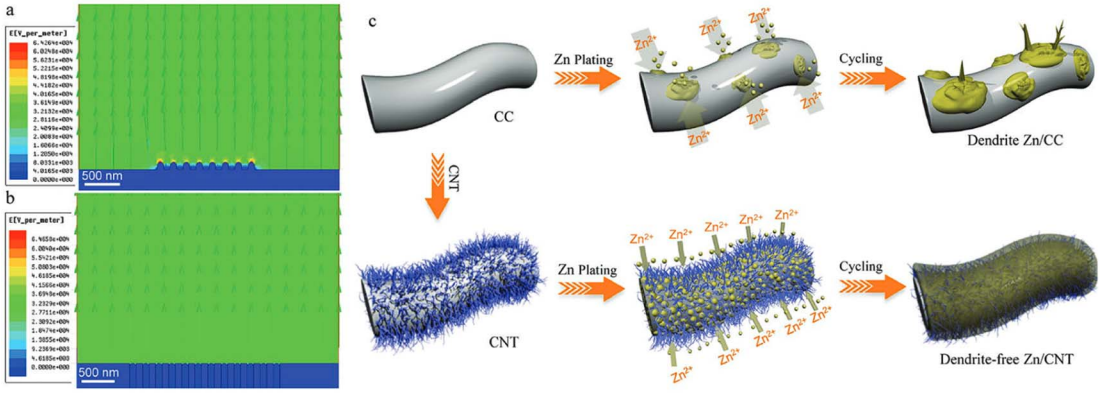

Fig. 2 Electric field distributions after Zn nucleation for (a) Zn/carbon cloth and (b) Zn/CNT anodes. (c) Illustration of Zn deposition on both anodes. Reproduced from ref. 72, with permission. Copyright 2019, Wiley.

nuclei. This gradient, after several cycling processes, results in Zn dendrites growing as demonstrated in Fig. 2c. The promising Zn/CNT anode was used in Zn/MnO_2 batteries, demonstrating a capacity retention of 88.7% after 1000 cycles with high mechanical flexibility.

Li and Sun[60] evaluated the electric field distribution and local current density at the anode/electrolyte interface using a vertical graphene carpet on commercial glass fiber Janus separators. Based on Sand's time mode, the initial formation of dendrites can be retarded by reducing the local current density.[73,74] The higher surface area of vertical graphene can reduce the current density from 1 to 0.24 mA cm^{-2} being better when compared to 2D planar graphene (0.38 mA cm^{-2}). The ion concentration field and electric field were theoretically evaluated by Yang and Guo[75] to inhibit dendrite formation using an artificial interface layer (hydrogen-substituted graphdiyne (HsGDY)). The electrode with an artificial interface layer presented a uniform concentration field on the Zn interface after 5 and 10 s of diffusion time and a homogeneous electric field, as presented in Fig. 3.

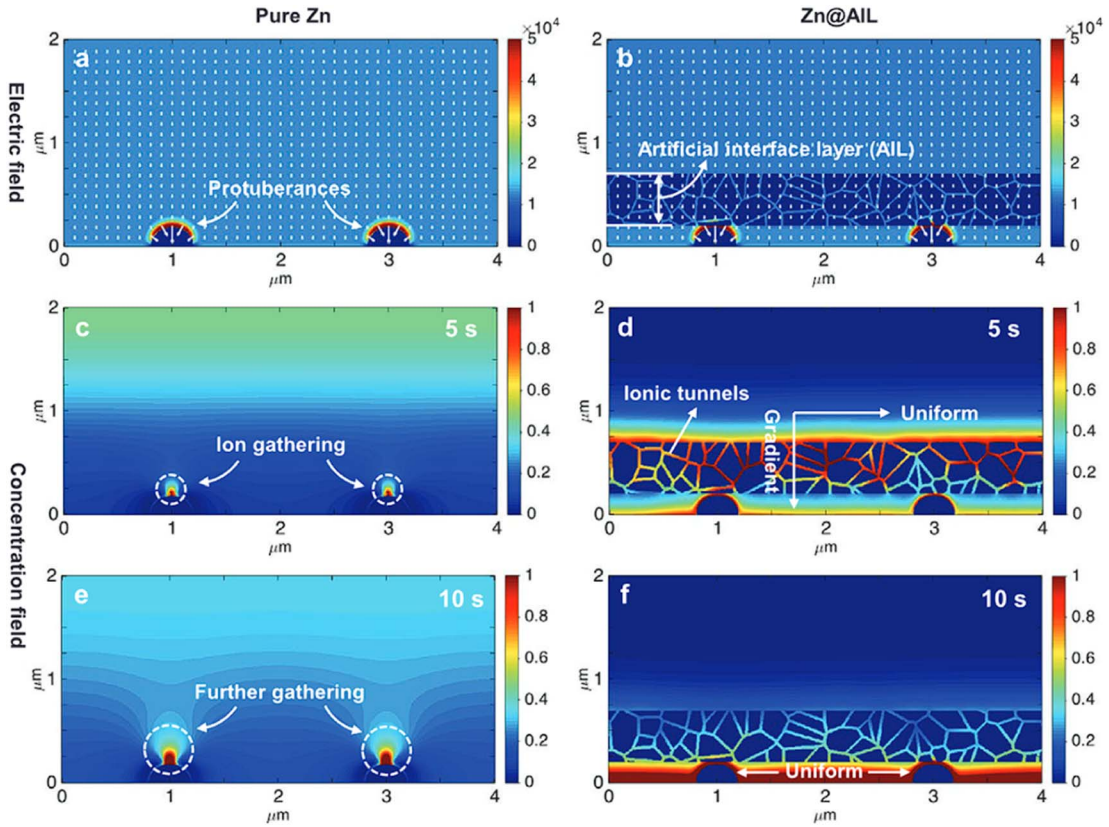

Fig. 3 Simulated electric field on (a) Zn electrode and (b) Zn with an artificial interface layer. (c–f) The concentration field of Zn^{2+} over the two electrodes at diffusion times of 5 s and 10 s. Reproduced from ref. 75, with permission. Copyright 2020, Wiley.

2.2. Materials for separators on zinc–manganese oxide batteries

In rechargeable alkaline Zn/MnO_2 batteries, the formation of an inactive zinc manganese spinel phase poisoning the cathode can lead to failure mechanisms mainly at high DOD.[46] Preventing the formation of zincate ($(Zn(OH)_4)_4^{2-}$) anions remains a significant difficulty for ensuring high energy density Zn/MnO_2 batteries.[32,33]

3D zinc anodes can mitigate dendrite problems as shown in the study by Parker and Chervin[76] where monolithic sponge electrodes allow the DOD to be increased at longer cycles. The current density influences the formation of dendrites with the dissolution being enhanced by the decrease of the current density.[77] Other approaches to decrease the formation of dendrites are using inorganic[78] and polymer coatings.[79]

The separator is an essential component of the battery systems since it works as an electrolyte contender to mediate the transport of ions and, at the same time, prevent the electron mobility.[80,81]

Several strategies have been implemented to improve the performance of rechargeable AZIBs by improving the separator properties such as controlling the cathode material dissolution (adsorbing the active material) and suppressing dendrite growth using a homogeneous electric field on the anode surface.[82] High mechanical strength and fatigue resistance are required for the separator layer to accumulate repeated cycles and suppress metal dendrite growth. The size and density of the pores are relevant to create a homogeneous ion flux between electrodes to obtain a stable Zn deposition at the anode/separator interface. Furthermore, the separator selectivity for the ion transportation also plays an important role since Zn^{2+} transport can be improved by the cathode species diffusivity, leading to the contamination of the anode. The separator needs to be inert to oxidation and reduction at the working voltage with no reaction with the active materials.

Typically, commercial primary alkaline Zn/MnO_2 batteries use glass fiber separators and nonwoven separators with a paper-like structure, combining layers of cellulose fibers with synthetic fibers based on nylon, rayon or polyvinyl alcohol.[83,84] In nonwoven membranes, the electrolyte absorbance can be enhanced using laminated cellophane, allowing OH^- consumption to be improved during the discharging process.[85]

2.2.1. Glass fiber. Considering aqueous electrolytes, the most used separator is based on commercial glass fiber (GF) due to its high porosity, high wettability and good chemical stability.[82] However, the high price, low tensile strength (0.25–0.5 MPa)[86,87] and high thickness ($\approx$300 μm),[86] which lead to a decrease in the volumetric energy and enhance the deposition of unstable Zn on the anode, limit its applicability for large-scale production.[88]

Separator modifications to improve separator–electrolyte and separator–anode interfaces have also been explored.[59,89,90] Since the separator is typically an inert component, the chemical and morphological modification using functionalization or surface coating allows battery performance to be improved.[91,92] The manipulation of the ionic and electronic conductivity of GF has been extensively studied in zinc ion batteries due to its suitable porosity, low electrical conductivity, and compatibility with aqueous electrolytes.[89,93] The short circuit of the battery has been observed for larger and non-uniform pore structures within GF separators due to lower ionic conductivity which induces faster dendrite growth.[94,95] Cao and Zhang[93] developed Janus separators based on a layer of graphene oxide as an interface between the glass fiber separator and the anode to successfully guide the preferential growth of Zn metal. Moreover, Qin and Liu[89] developed a distinct Janus separator by chemical vapor deposition to vertically grow graphene carpets to obtain a more uniform electric field distribution which led to a more uniform Zn deposition.

Song and Ruan[96] developed a glass fiber separator with UiO-66 MOFs deposited *via* a hydrothermal process, showing Zn stripping/plating for 1650 h at 2 mA cm^{-2} for 1 mA h cm^{-2}. An abundant pore structure and large specific surface area were obtained with a uniform distribution of the electric field. A full cell presented a capacity retention of 85% after 1000 cycles at 1 A g^{-1}.

Yang and Wu[97] developed a glass fiber separator coated with a covalent organic framework by the solvothermal growth reaction, presetting polar functional groups and improving electronegativity, which lead to increasing ion diffusion but also dendrite growth. An overpotential of 91.5 mV was achieved for more than 1500 h at a large current density of 10.0 mA cm^{-2}. Capacities higher than 200 mA h g^{-1} were obtained for a full battery after 700 cycles at 1 A g^{-1}. Cao and Zhang[93] used graphene oxide on glass fiber using a vacuum filtration method to develop a separator capable of preferential growth of crystal plane orientation and constant Zn nucleation. A capacity fade over 500 cycles of less than 25% at 0.5 A g^{-1} was achieved and the full battery exhibits a specific capacity of 126 mA h g^{-1} at 0.1 A g^{-1} and high-power density of 20.8 kW kg^{-1}.

Commercial glass fiber was sprayed with $Ti_3C_2T_x$ ink to produce a Janus separator with 960 μm of thickness capable of inhibiting dendrite growth, showing a stable overpotential of 25.1 mV after 2000 h at 1 mA cm^{-2} and a capacity retention of 86.7% after 500 cycles at 1 A g^{-1}.[98] Lin and Zhou[99] developed a glass fiber separator with spray sonicated Ketjen black and zinc oxide nanoparticles to obtain a thickness of 293 μm, capable of homogenizing the electric field at the anode interface, contributing to a uniform Zn growth, stable at 1 mA cm^{-2} for 2218 h. The full battery presented a specific capacity of $\approx$100 mA h g^{-1} after 995 cycles at 0.3 A g^{-1} (Fig. 4a). The modification of commercial glass fibers using graphite fluoride nanoflakes *via* vacuum filtration presented high zinc affinity, reducing the by-products and dendrite growth.[100] Stable cycles were observed at 1 mA cm^{-2} and 5 mA cm^{-2} for 1800 h and 900 h, respectively. A full battery could deliver 1 A g^{-1} at a capacity retention of 92% after 200 cycles, as presented in Fig. 4b.

Huang and Zhou[101] developed a separator based on glass fiber sprayed with Ketjen black on the cathode side, capable of improving the diffusivity and suppressing cathode dissolution. A specific capacity of 194.6 mA h g^{-1} was obtained at 2 A g^{-1} after 1500 cycles and a capacity retention of 87% was observed at 5 A g^{-1} after 6000 cycles.

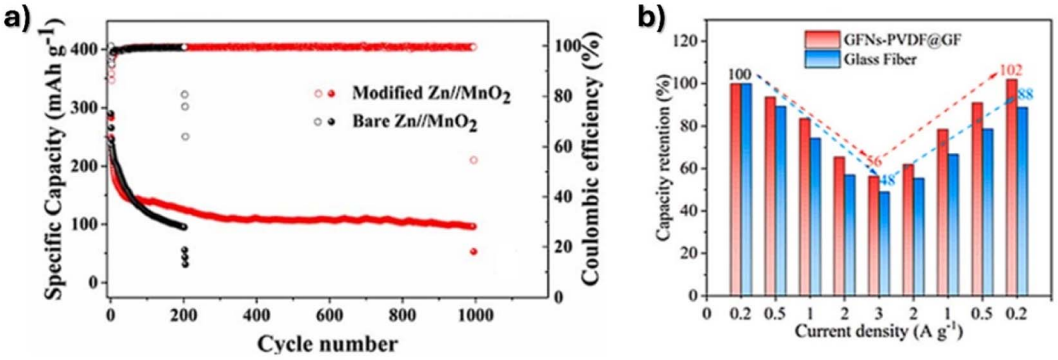

Fig. 4 Cycling performance of (a) glass fiber separator with spray sonicated Ketjen black and zinc oxide nanoparticles. Reproduced from ref. 99, with permission. Copyright 2023, Royal Society of Chemistry and (b) capacity retention of commercial glass fibers with graphite fluoride nanoflakes. Reproduced from ref. 100, with permission. Copyright 2023, Elsevier.

Graphene sheets with sulfonic cellulose were spin-coated on commercial GF to produce a Janus separator capable of regulating the Zn (002) crystallographic orientation by repelling SO_4^{2-} and attracting H^+ to reduce the side reactions. A capacity retention of 95% after 1900 cycles at 1 A g^{-1} was obtained for a Zn/CNT/MnO_2 cell. An aqueous pouch cell based on Zn/$NH_4V_4O_{10}$ presented a capacity of 157 mA h g^{-1}, corresponding to a capacity retention of 87.4% at 2 A g^{-1} after 260 cycles.[102]

A prolonged performance up to 500 h was obtained by regulating the Zn deposition and inhibition of dendrite growth using a Sn-coated separator at 10 mA cm^{-2}.[59] The discharge capacity after 600 cycles was 200 mA h g^{-1} at 0.3 A g^{-1}. A dendrite-free Zn anode based on MXene nanoporous NiO heterostructures with an areal capacity of 10 mA h cm^{-2} and stable cyclability over 500 h was reported in ref. 103.

It has also been demonstrated that metal–organic frameworks (MOFs) as coatings restrict the Zn^{2+} flux and consequently dendrite formation,[97,104] mainly through the combination of inorganic metals and organic ligands showing high resistance to acid and alkaline electrolytes.[105–107] The modification of the size of the organic ligands allows ion diffusion channels to be tuned to specific sizes which facilitates Zn^{2+} ion diffusion.[108] MOFs also allow water activity in the electrolyte to be regulated by introducing functional groups capable of producing hydrogen bond networks.[109,110]

2.2.2. Cellulose-based materials. There are also other materials applied to AZIBs such as lignocellulose from biomass and different polymers due to their tailorable properties. The performance of lignocellulose-based separators can be improved by surface coating[111] and grafting functional groups.[112] Ma and Yu[113] developed a lignocellulose separator functionalized with Zr-based MOFs (UiO-66-NH_2) with 20 μm of thickness, demonstrating a 2000 h working life at 2 mA cm^{-2} and remaining operational with an area capacity of 25 mA h cm^{-2}. A high tensile strength of 47.4 MPa and ionic conductivity of 17.2 mS cm^{-1}, hydrophilic behavior and mechanical flexibility were observed, allowing batteries with a capacity retention of 95.1% after 1000 cycles. The lignin low solubility in several solvents promoted the development of neat cellulose-based separators with good mechanical strength and low cost.[114] Cellulose-based separators, due to their oxygen groups, large mechanical strength, good wettability and natural origin are promising materials to substitute glass fiber separators.[115,116] Furthermore, high thickness cellulose-based separators prevent the short circuit due to dendrite growth, but decrease energy density.[91]

A separator obtained from cellulose fibers on cotton presented a tensile strength and modulus of 29.2 MPa and 4.16 GPa, respectively with a high concentration of hydroxyl groups on a dense and uniform nanoporous structure.[91] Cellulose nanofibrils have also been obtained from algae showing a dense and uniform mesopore structure with a size of ≈20 nm.[117] The performance of cellulose separators can be improved by grafting sulfonate groups, which enhance the Zn^{2+} conduction and regulate the cation flux, forming hydrogen bonds with water molecules of the electrolyte and leading to a reduction in the water reactivity.[118]

Zhou and Chen[91] developed a cotton-derived cellulose separator by vacuum filtration with a thickness of 140 μm, a high ionic conductivity of 56.95 mS cm^{-1} and a tensile strength of 29.2 MPa. This separator presents a network of dense and uniform nanopores with hydroxyl groups, reducing the zinc nucleation overpotential (≈105 mV over 2000 h), which increases the zinc ion transfer number, accelerates zinc deposition and suppresses the side reactions. The zinc plating capacity of Zn//Zn cells reached 1000 mA h cm^{-2} and 850 mA h cm^{-2} at 1 mA cm^{-2} and 2 mA cm^{-2}, respectively. Fig. 5a shows the morphology of this separator applied to a Zn/MnO_2 battery, obtaining a capacity retention of 63.6% after 1000 cycles at 1 A g^{-1}. An ultrathin (9 μm) and high-toughness membrane based on bacterial cellulose presenting a tensile strength of 120 MPa showed a chemical affinity to the Zn(100) crystal plane (Fig. 5b), with the hydroxyl groups leading to inhibition of dendrite growth and corrosion suppression and the battery being stable over 4000 h at 0.5 mA cm^{-2} within 0.1 mA h cm^{-2}.[119] The Zn/MnO_2 battery presents a specific capacity of 171.7 mA h g^{-1} after 100 cycles at a 1C rate as presented in Fig. 5c.

Solution cast separators based on cellulose nanofibers–ZnO_2 composites presented an ionic conductivity of 4.59 mS cm^{-1},

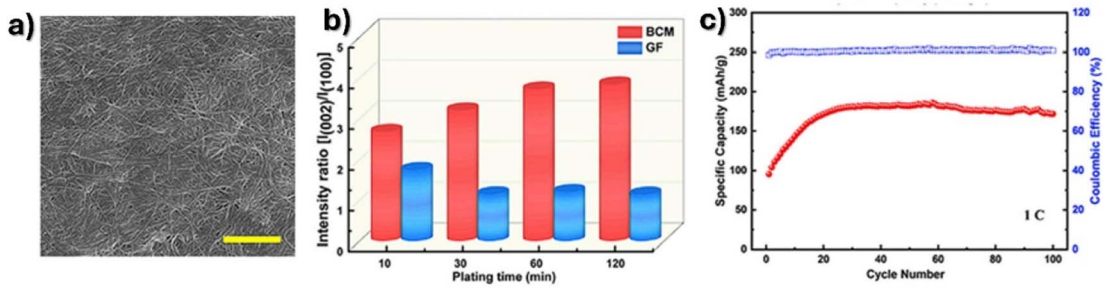

Fig. 5 (a) SEM images of a cycled bacterial cellulose based separator; (b) intensity ratio of crystal planes from Zn plating and (c) stability of the battery at 1C. Reproduced from ref. 119, with permission. Copyright 2022, Cell Press.

a Zn^{2+} transfer number of 0.69 and a dielectric constant of 25.[115] The separator showed high Zn^{2+} diffusion while repelling anions, with the uniform Zn deposition leading to inhibition of dendrite growth with an overpotential of 57 mV over 2000 h at 0.5 mA cm^{-2}. A full battery capacity retention of 87.2% was achieved at 2.5 A g^{-1} over 3000 cycles. Yang and Wu[112] modified a conventional filter paper to produce a cellulose-based separator with preferential adsorptions of protons, sulfate, and zinc ions, to inhibit dendrite growth as presented in Fig. 6a. A stable performance was obtained at a current density of 5 mA cm^{-2} over 2900 h and a full battery capacity retention of 98.4% after 1000 cycles at 1 A g^{-1} was obtained (Fig. 6b). Furthermore, Liu and Kong[111] also developed a separator based on filter paper with strontium titanate coating (Fig. 6c) with an overall thickness of 46 μm, presenting enhanced dielectric properties. A specific capacity higher than 80 mA h g^{-1} has been obtained for a full battery after 300 cycles at 0.5 A g^{-1} for a new separator based on a strontium titanate ($SrTiO_3$) coating, which presents high specificity that allows homogenizing the ion flow (Fig. 6d).

A commercial cotton towel was used as a separator for aqueous zinc-ion batteries (AZIBs), presenting good mechanical performance (tensile strength of 6 MPa) and a thickness of 415 μm with high wettability, suppressing side reactions and dendrite growth.[120] A lifespan of 700 h at 2 mA cm^{-2} for 4 mA h cm^{-2} was achieved, with the full cell presenting a cyclability of 96.9 mA h g^{-1} after 2400 cycles at 3 A g^{-1}.

2.2.3. Synthetic polymer-based materials. Polymer-based separators, due to their tailorable properties to improve chemical and thermal stability and mechanical strength, are already applied for LIBs, and the same strategy is used to improve AZIBs.[121,122] High proton conductivity Nafion-based polymeric membrane,[123] which was used in lithium–sulfur batteries, leading to a high electrostatic repulsion between the polysulfides and functional groups enhancing the lithium-ion transport,[124,125] has been recently used in AZIBs. High ionic conduction and Zn transfer have been obtained by immersing the Nafion membranes into Zn electrolyte which allows Zn^{2+} transportation.[126] Wu and Wu[127] theoretically evaluated Nafion separators, showing a steady Zn deposition due to the homogeneous electric and Zn ion concentration fields.

Ghosh and Vijayakumar[128] developed a Zn/MnO_2 cell with a Nafion ionomer separator combined with zinc ion conductive electrolytes to improve the capacity retention up to 75% over 1000 cycles.

A *N*-butylimidazolium-functionalized polysulfone separator (50 wt% concentration) presented a comparable overall

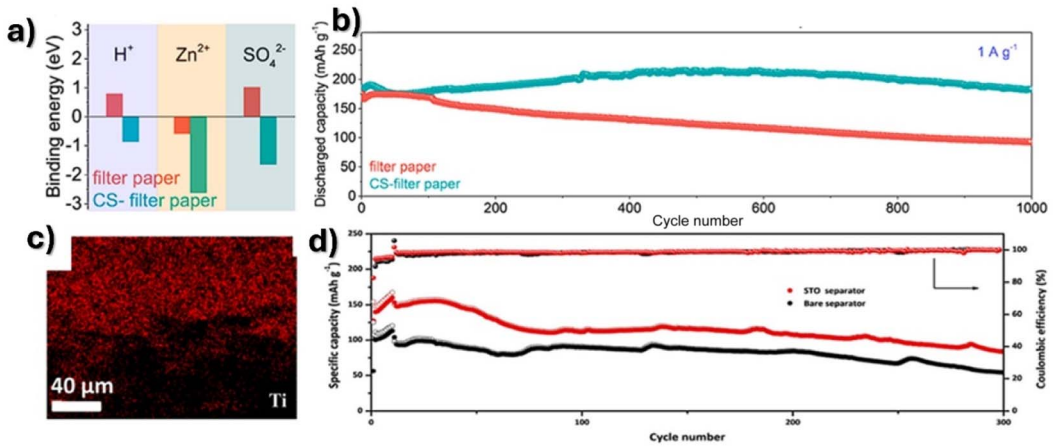

Fig. 6 (a) Zinc, proton and sulfate ion adsorption and (b) cycling performance of cellulose-based separators. Reproduced from ref. 112, with permission. Copyright 2022, Elsevier. (c) SEM image of strontium titanate distribution in filter paper separators and (d) the cycling performance at 0.5 A g^{-1}. Reproduced from ref. 111, with permission. Copyright 2023, Elsevier.

conductivity and hydroxide diffusivity but also lower permeability to zincate when compared to commercial separators.[129] This separator was evaluated in a Zn/MnO_2 battery, showing an extended lifetime from 21 to 79 cycles for two-electron capacity after falling to 50%.

Also in the scope of polymer-based separators, polyacrylonitrile electrospun fibers with a thickness of 69 μm present a tensile strength of 3.62 MPa with enhanced bending movement and excellent pore connectivity,[130] leading to a higher regulation of cation transport due to the uniform ion flux and electrostatic interaction between nitrogen and Zn. Another promising polymer for battery applications is poly(-vinylidene fluoride), PVDF, which presents low ionic conductivity and poor hydrophilicity. Liu and Liu[87] coated a polydopamine surfactant leading to a uniform Zn deposition on the PVDF nanofiber surface.

Poly(vinylidene fluoride-*co*-hexafluoropropylene), PVDF-HFP, polymer matrix composites with catalytic ions (manganese sulfate, $MnSO_4$, zinc trifluoromethanesulfonate, $Zn(OTf)_2$, 1-ethyl-3-methylimidazolium bis(trifluoromethylsulfonyl)imide ([EMI-TFSI]IL) and ionic liquids) facilitate the acceleration of zinc ion deposition and migration kinetics, as well as enhance charge transfer at the electrode/electrolyte interface.[131] A Zn/MnO_2 battery with a PVDF composite separator with the IL $PPCu_1C\text{-}ZMIL_5$ showed a specific capacity of 124.6 mA h g^{-1} at a 1C rate over 1000 cycles (Fig. 7a). The separators developed by Liang and Ma[132] based on PVDF/barium titanate composites can efficiently capture and facilitate the Zn^{2+} transport at the electrolyte–electrode interface and redistributes the ion transport to achieve improved homogeneity at the separator–anode interface. A specific capacity of 108 mA h g^{-1} at 1 A g^{-1} after 1800 cycles was achieved presenting a capacity retention improvement of 115% at 0.2 A g^{-1} after 100 cycles as presented in Fig. 7b.

A stretchable Zn/MnO_2 battery with a biocompatible separator based on poly(styrene-isobutylene-styrene) (SIBS) presented an ionic conductivity of 0.05 S m^{-1} with a specific capacity of 160 mA h g^{-1} and capacity retention of 75% after 500 charge and discharge cycles.[133] The developed battery also presents functionality after 150 cycles when a strain of 100% was applied.

The utilization of nanofibrous polymers with additives allows the formation of size dependent conductive pathways which facilitate the diffusion of hydroxide ions (small size) over the zincate ions (larger size). Huang and Yadav[134] developed an ion-selective composite membrane based on graphene oxide/poly(vinyl alcohol) to suppress the zincate ion while the conduction of hydroxyl ions remains constant. The primary and secondary cells showed an area capacity of 20 mA h cm^{-2} for a near full MnO_2 two-electron capacity (617 mA h g^{-1}). The advanced separator reached three times higher cycle life (300) when compared to zincate blocking separators.

A flexible Zn/MnO_2 battery was fabricated using a dual-crosslinked Zn-alginate/PAAm hydrogel electrolyte showing a specific capacity of 300.4 mA h g^{-1} at 0.11 A g^{-1} with a capacity retention of 82% at 0.88 A g^{-1} after 500 charge and discharge cycles. The battery also presents capability of supporting high mechanical stresses such as a car run-over for 20 times for 2 days.[135]

2.2.4. Ceramic-based materials and printed batteries. Commercial separators based on NASICON with thicknesses of 1 and 0.5 mm were evaluated to increase the cycle lifetime of an alkaline Zn/MnO_2 battery with a NaOH electrolyte. The increase in thickness leads to an increase in electrical resistance from 10 Ω to 25 Ω for low C-rates. The thinner separator increases the cycle lifetime by 22% at a C/5 rate with impermeability to zincate anions, preventing battery failure.[34] The use of a calcium hydroxide ($Ca(OH)_2$) sheet between the anode and separators (Fig. 8a) of Zn/MnO_2 batteries allows the $(Zn(OH)_4)_4^{2-}$ concentration to be effectively reduced at a DOD of 100% and in 60 cycles, presenting a capacity retention of 90 mA h g^{-1} as presented in Fig. 8b.[46] $Ca(OH)_2$ presents a reversible reaction with zincate ions, forming insoluble calcium zincate ($Ca(OH)_2 \cdot 2Zn(OH)_2 \cdot 2H_2O$),[136,137] improving the performance and longevity of the batteries by trapping zincate ions.[46]

Furthermore, printed Zn/MnO_2 batteries have also been developed. A printable and flexible Zn/MnO_2 battery with a hydrogel separator with a specific capacity of 7.3 mA h cm^{-2} was reported in ref. 138. A printed planar micro-battery with neutral aqueous electrolyte was reported in ref. 139 based on interdigitated Zn and MnO_2 ink patterns. The separator-free battery achieved a capacity of 393 mA h g^{-1} at 7.5 mA cm^{-3} and a capacity retention of 83.9% at 5C after 1300 cycles with high mechanical flexibility and capacity stability under several

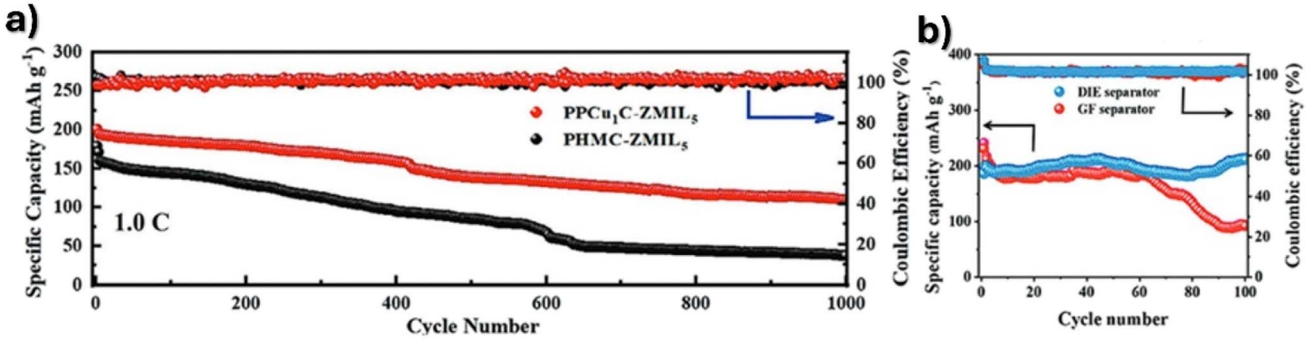

Fig. 7 Cycling performance of PVDF composite-based separators with (a) ionic liquid $PPCu_1C\text{-}ZMIL_5$. Reproduced from ref. 131, with permission. Copyright 2022, Wiley and (b) barium titanate nanoparticles. Reproduced from ref. 132, with permission. Copyright 2022, Wiley.

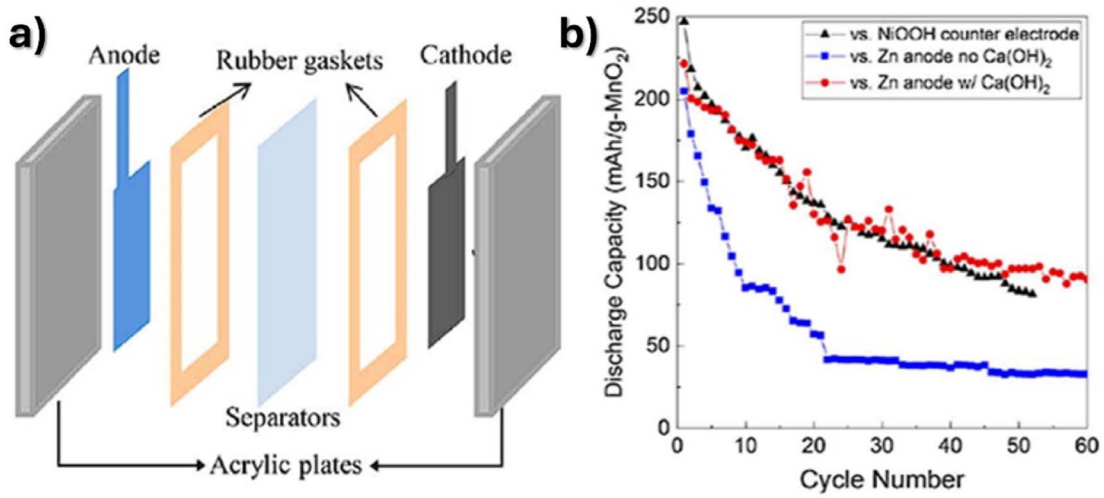

Fig. 8 (a) Schematic representation of a Zn/MnO_2 battery with a calcium hydroxide sheet between electrodes and (b) discharge capacity over cycling. Reproduced from ref. 46, with permission. Copyright 2017, Elsevier.

deformations. A capacity retention of 83% over 900 cycles was obtained using a calcium hydroxide layer.[42]

Typically, the most commonly used separator for this battery system is glass fiber, whose manufacturing process is relatively simple and scalable and, consequently, presents low production costs. These separators are flexible, but they are not mechanically strong enough to withstand pressure and stresses during battery operation. The main disadvantage is the limited chemical compatibility, which must be improved both with the electrolyte and electrodes to avoid degradation and improve ionic conductivity. Separators based on cellulose and other synthetic polymers have some advantages over glass fiber separators, with the main disadvantage being the cost. This issue must be addressed for their future implementation in commercial batteries.

Overall, it is shown that Zn/MnO_2 batteries are a potential alternative to lithium-ion batteries for some applications considering the cost and capacity value, but more work is needed to solve dendrite growth and electrode/electrolyte interfaces, among others.

These issues in the separator membrane have been studied using different coatings, but more work is needed, together with the proper engineering of the interface with the electrodes.

For this, it is essential to improve separator materials to obtain high-performance electrochemical energy storage devices.

3. Final remarks and future needs

The key advances in the scope of separator materials and technologies and theoretical simulations for zinc–manganese oxide batteries have been presented. This energy storage system has strong potential for the next generation of high-performance energy storage devices, which aim to replace some critical minerals of lithium-ion batteries, such as lithium, cobalt and nickel, with more available and environmentally friendly materials, including zinc and magnesium.

Those batteries will allow a high discharge capacity value to be obtained but present a low voltage, being suitable for specific application areas, such as wearable and related portable devices.

Nevertheless, in order to reach their full potential, electrode interfaces have to be improved and dendrite growth issues have to be solved.

In order to overcome these issues, particular attention must be paid to the separator membrane and electrode/electrolyte interfaces. The most popular separator for this kind of battery is typically made of nonwoven materials, but it also needs to be improved in terms of its mechanical, electrochemical, and thermal characteristics. Utilizing composites based on metal–organic frameworks (MOFs), zeolites, and other ceramics that inhibit dendritic development may allow the mechanical and thermal properties to be improved, combined with coating layers.

In order to investigate synergistic effects and attain flame retardant behavior, wettability, dimensional stability, interface compatibilization, and dendritic growth suppression, innovative ways combining various materials in a separator type are required.

Furthermore, it is necessary to use new types of polymers including UV curing polymers, allowing the interfaces between components to be reduced, obtaining dendrite-free batteries. Additionally, theoretical simulations are essential to go beyond trial-and-error experimental work. In this scope, extensive work on the interfacial electrochemical processes at the separator–electrolyte and separator–anode interfaces is required. These issues such as separator morphology, new electrolyte solutions and their respective compatibility with porous membranes and the use of additive manufacturing techniques for improved battery scalability are necessary in this field.

Separator materials play a significant and critical role in zinc–manganese oxide batteries, where new scientific and technological developments are required in this field to improve the thermal, mechanical, and electrochemical

properties in order to obtain high-performance batteries allowing LIBs and their critical materials to be replaced in specific applications, thus contributing to improved performance and sustainability.

Conflicts of interest

There are no conflicts to declare.

Abbreviations

List of symbols

a	Electrode area per volume [cm^{-1}]
c_i	Concentration [mol m^{-3}]
D_a	Electrolyte effective diffusion coefficient [cm^2 s^{-1}]
$D_{a,\infty}$	Bulk electrolyte diffusion coefficient [cm^2 s^{-1}]
F	Faraday constant [C mol^{-1}]
H	Height [cm]
i_0	Exchange current density [A cm^{-2}]
i_1	Current density of the solid phase [A cm^{-2}]
i_2	Current density of electrolyte [A cm^{-2}]
i_n	Normal current density at the pore wall interface [A cm^{-2}]
I	Discharge current density [A cm^{-2}]
j_{in}	Solid phase to solution pore wall flux [mol m^{-2} s^{-1}]
j	Transfer current density per volume [A cm^{-3}]
L	Length of the electrode [m]
N_i	Superficial ionic flux on the porous electrode [mol m^{-2} s^{-1}]
N	Total number of cathode particles
n	Number of electrons in the electrochemical reaction
r_0	Outer radius of cathode particles [cm]
R_i	Production rate of each species by the electrochemical reaction
R	Universal gas constant [J K^{-1} mol^{-1}]
s_i	Stoichiometric coefficient of the electrochemical reaction
$t_i^{'}$	Transference number
T	Temperature [K]
v'	Flow velocity
V_0^-	Water molar volume [cm^3 mol^{-1}]
V_a^-	Electrolyte molar volume [cm^3 mol^{-1}]
V_α^-	Molar volume of α-MnOOH [cm^3 mol^{-1}]
V_γ^-	Molar volume of γ-MnOOH [cm^3 mol^{-1}]
W	Width [cm]

Greek symbols

α_a	Anodic transfer coefficient
α_c	Cathodic transfer coefficient
ε	Porosity of electrodes
η	Overpotential [V]
κ_∞	Bulk electrolyte conductivity [S cm^{-1}]
κ	Electrolyte conductivity [S cm^{-1}]
σ	Electrode conductivity [S cm^{-1}]
ϕ_1	Potential of the solid phase [V]
ϕ_2	Potential of electrolyte [V]

Acknowledgements

The authors thank the Fundação para a Ciência e Tecnologia (FCT) for financial support under the framework of Strategic Funding UIDB/05549/2020, UIDP/05549/2020 Applied Artificial Intelligence Laboratory (2Ai), UIDB/04650/2020, UID/FIS/04650/2020, UID/04650 Physics Centre of Minho and Porto Universities (CF-UM-UP), UID/EEA/04436/2020, LASI-LA/P/0104/2020 and UID/QUI/00686/2020 and under projects, POCI-01-0247-FEDER-046985 and 10.54499/2022.03931.PTDC funded by national funds through FCT and by the ERDF through the COMPETE2020—Programa Operacional Competitividade e Internacionalização (POCI) and project SmartHealth, "NORTE-01-0145-FEDER-000045", supported by the Northern Portugal Regional Operational Programme (Norte2020), under the Portugal 2020 Partnership Agreement, through the European Regional Development Fund (ERDF) and NGS-New Generation Storage, C644936001-00000045, supported by IAPMEI (Portugal) with funding from the European Union NextGenerationEU (PRR). The authors also thank the FCT for financial support under UMINHO/BIPD/2024/4 (J. C. B.) and FCT investigator contracts CEECIND/00833/2017 (DOI: 10.54499/CEECIND/00833/2017/CP1458/CT0017) (RG) and 2020.04028.CEECIND (DOI: 10.54499/2020.04028.CEECIND/CP1600/CT0018) (C. M. C.). This study forms part of the Advanced Materials program and was supported by MCIN with funding from the European Union NextGenerationEU (PRTR-C17.I1) and by the Basque Government under the IKUR program.

References

1 C. M. Costa, J. C. Barbosa, R. Gonçalves, H. Castro, F. J. Del Campo and S. Lanceros-Méndez, *Energy Storage Mater.*, 2021, **37**, 433–465.
2 M. B. Lim, T. N. Lambert and B. R. Chalamala, *Mater. Sci. Eng., R*, 2021, **143**, 100593.
3 T. Prior, P. A. Wager, A. Stamp, R. Widmer and D. Giurco, *Sci. Total Environ.*, 2013, **461–462**, 785–791.
4 G. Martin, L. Rentsch, M. Höck and M. Bertau, *Energy Storage Mater.*, 2017, **6**, 171–179.
5 I. Y. L. Hsieh, M. S. Pan, Y. M. Chiang and W. H. Green, *Appl. Energy*, 2019, **239**, 218–224.
6 J. Y. Luan, H. Y. Yuan, J. Liu and C. Zhong, *Energy Storage Mater.*, 2024, **66**, 103206.
7 G. G. Yadav, D. Turney, J. C. Huang, X. Wei and S. Banerjee, *ACS Energy Lett.*, 2019, **4**, 2144–2146.
8 J. B. Miao, Y. X. Du, R. T. Li, Z. K. Zhang, N. N. Zhao, L. Dai, L. Wang and Z. X. He, *Int. J. Miner., Metall. Mater.*, 2024, **31**, 33–47.
9 N. Guo, Z. Peng, W. Huo, Y. Li, S. Liu, L. Kang, X. Wu, L. Dai, L. Wang, S. C. Jun and Z. He, *Small*, 2023, **19**, e2303963.
10 P. Marsal, R. River, K. Kordesch and L. Urry, Dry Cell, *US Pat.*, 2960558, 1960.
11 Y. L. Zhao, Y. H. Zhu and X. B. Zhang, *InfoMat*, 2020, **2**, 237–260.

12 D. Miranda, C. M. Costa and S. Lanceros-Mendez, *J. Electroanal. Chem.*, 2015, **739**, 97–110.
13 C. Li, R. Zhang, H. L. Cui, Y. B. Wang, G. J. Liang and C. Y. Zhi, *Trans. Tianjin Univ.*, 2024, **30**, 27–39.
14 R. Durena and A. Zukuls, *Batteries*, 2023, **9**, 311.
15 B. Dunn, H. Kamath and J. M. Tarascon, *Science*, 2011, **334**, 928–935.
16 A. R. Dehghani-Sanij, E. Tharumalingam, M. B. Dusseault and R. Fraser, *Renewable Sustainable Energy Rev.*, 2019, **104**, 192–208.
17 J. B. Goodenough and Y. Kim, *Chem. Mater.*, 2009, **22**, 587–603.
18 D. Chao, W. Zhou, F. Xie, C. Ye, H. Li, M. Jaroniec and S. Z. Qiao, *Sci. Adv.*, 2020, **6**, eaba4098.
19 J. H. Huang, Z. W. Guo, Y. Y. Ma, D. Bin, Y. G. Wang and Y. Y. Xia, *Small Methods*, 2019, **3**, 1800272.
20 L. E. Blanc, D. Kundu and L. F. Nazar, *Joule*, 2020, **4**, 771–799.
21 C. P. Li, X. S. Xie, S. Q. Liang and J. Zhou, *Energy Environ. Mater.*, 2020, **3**, 146–159.
22 T. Xue and H. J. Fan, *J. Energy Chem.*, 2021, **54**, 194–201.
23 L. J. Yan, X. M. Zeng, Z. H. Li, X. J. Meng, D. Wei, T. F. Liu, M. Ling, Z. Lin and C. D. Liang, *Mater. Today Energy*, 2019, **13**, 323–330.
24 C. Wang, Y. X. Zeng, X. Xiao, S. J. Wu, G. B. Zhong, K. Q. Xu, Z. F. Wei, W. Su and X. H. Lu, *J. Energy Chem.*, 2020, **43**, 182–187.
25 *Part 273—Standards for Universal Waste Management*, 40 Cfr, 2017.
26 A. Biswal, B. C. Tripathy, K. Sanjay, T. Subbaiah and M. Minakshi, *RSC Adv.*, 2015, **5**, 58255–58283.
27 A. M. Popov, M. O. Kozhnov, T. A. Labutin, S. M. Zaytsev, A. N. Drozdova and N. A. Mityurev, *Tech. Phys. Lett.*, 2013, **39**, 81–83.
28 I. Gyuk, M. Johnson, J. Vetrano, K. Lynn, W. Parks, R. Handa, L. Kannberg, S. Hearne, K. Waldrip and R. Braccio, *Grid Energy Storage*, U.S. Department of Energy, 2013.
29 C. Liu, X. Wang, W. Deng, C. Li, J. Chen, M. Xue, R. Li and F. Pan, *Angew Chem. Int. Ed. Engl.*, 2018, **57**, 7046–7050.
30 M. H. Alfaruqi, J. Gim, S. Kim, J. Song, J. Jo, S. Kim, V. Mathew and J. Kim, *J. Power Sources*, 2015, **288**, 320–327.
31 Y. Zeng, X. Zhang, Y. Meng, M. Yu, J. Yi, Y. Wu, X. Lu and Y. Tong, *Adv. Mater.*, 2017, **29**, 1700274.
32 J. W. Gallaway, B. J. Hertzberg, Z. Zhong, M. Croft, D. E. Turney, G. G. Yadav, D. A. Steingart, C. K. Erdonmez and S. Banerjee, *J. Power Sources*, 2016, **321**, 135–142.
33 J. W. Gallaway, M. Menard, B. Hertzberg, Z. Zhong, M. Croft, L. A. Sviridov, D. E. Turney, S. Banerjee, D. A. Steingart and C. K. Erdonmez, *J. Electrochem. Soc.*, 2015, **162**, A162–A168.
34 J. Duay, M. Keny and T. N. Lambert, *J. Power Sources*, 2018, **395**, 430–438.
35 D. Im, A. Manthiram and B. Coffey, *J. Electrochem. Soc.*, 2003, **150**, A1651–A1659.
36 M. Kelly, J. Duay, T. N. Lambert and R. Aidun, *J. Electrochem. Soc.*, 2017, **164**, A3684–A3691.
37 N. D. Ingale, J. W. Gallaway, M. Nyce, A. Couzis and S. Banerjee, *J. Power Sources*, 2015, **276**, 7–18.
38 M. R. Bailey and S. W. Donne, *Electrochim. Acta*, 2011, **56**, 5037–5045.
39 D. E. Turney, J. W. Gallaway, G. G. Yadav, R. Ramirez, M. Nyce, S. Banerjee, Y. C. K. Chen-Wiegart, J. Wang, M. J. D'Ambrose, S. Kolhekar, J. C. Huang and X. Wei, *Chem. Mater.*, 2017, **29**, 4819–4832.
40 X. Wei, D. Desai, G. G. Yadav, D. E. Turney, A. Couzis and S. Banerjee, *Electrochim. Acta*, 2016, **212**, 603–613.
41 G. G. Yadav, J. W. Gallaway, D. E. Turney, M. Nyce, J. Huang, X. Wei and S. Banerjee, *Nat. Commun.*, 2017, **8**, 14424.
42 G. G. Yadav, X. Wei, J. Huang, J. W. Gallaway, D. E. Turney, M. Nyce, J. Secor and S. Banerjee, *J. Mater. Chem. A*, 2017, **5**, 15845–15854.
43 J. Duay, T. N. Lambert and R. Aidun, *Electroanalysis*, 2017, **29**, 2261–2267.
44 H. J. Lee, J. M. Lim, H. W. Kim, S. H. Jeong, S. W. Eom, Y. T. Hong and S. Y. Lee, *J. Membr. Sci.*, 2016, **499**, 526–537.
45 H. J. Hwang, W. S. Chi, O. Kwon, J. G. Lee, J. H. Kim and Y. G. Shul, *ACS Appl. Mater. Interfaces*, 2016, **8**, 26298–26308.
46 J. C. Huang, G. G. Yadav, J. W. Gallaway, X. Wei, M. Nyce and S. Banerjee, *Electrochem. Commun.*, 2017, **81**, 136–140.
47 M. B. Lim, T. N. Lambert and B. R. Chalamala, *Mater. Sci. Eng., R*, 2021, **143**, 100593.
48 U. Sengupta, S. Megahed, A. Homa and S. Ruth, *Proceedings of WESCON 1994 – Idea/Microelectronics, Conference Record*, Institute of Electrical and Electronics Engineers Inc., 1994, pp. 249–255.
49 M. Song, H. Tan, D. L. Chao and H. J. Fan, *Adv. Funct. Mater.*, 2018, **28**, 1802564.
50 D. Chao, W. Zhou, C. Ye, Q. Zhang, Y. Chen, L. Gu, K. Davey and S. Z. Qiao, *Angew Chem. Int. Ed. Engl.*, 2019, **58**, 7823–7828.
51 W. Li, B. Song and A. Manthiram, *Chem. Soc. Rev.*, 2017, **46**, 3006–3059.
52 P. K. Nayak, L. Yang, W. Brehm and P. Adelhelm, *Angew Chem. Int. Ed. Engl.*, 2018, **57**, 102–120.
53 C. Vaalma, D. Buchholz, M. Weil and S. Passerini, *Nat. Rev. Mater.*, 2018, **3**, 18013.
54 Y. M. Li, Y. X. Lu, C. L. Zhao, Y. S. Hu, M. M. Titirici, H. Li, X. J. Huang and L. Q. Chen, *Energy Storage Mater.*, 2017, **7**, 130–151.
55 Y. Yin, S. Wang, Q. Zhang, Y. Song, N. Chang, Y. Pan, H. Zhang and X. Li, *Adv. Mater.*, 2020, **32**, e1906803.
56 Z. Yi, G. Chen, F. Hou, L. Wang and J. Liang, *Adv. Energy Mater.*, 2020, **11**, 2003065.
57 A. Naveed, T. Rasheed, B. Raza, J. Chen, J. Yang, N. Yanna and J. Wang, *Energy Storage Mater.*, 2022, **44**, 206–230.
58 Y. Z. Chu, S. Zhang, S. Wu, Z. L. Hu, G. L. Cui and J. Y. Luo, *Energy Environ. Sci.*, 2021, **14**, 3609–3620.
59 Z. Hou, Y. Gao, H. Tan and B. Zhang, *Nat. Commun.*, 2021, **12**, 3083.
60 C. Li, Z. Sun, T. Yang, L. Yu, N. Wei, Z. Tian, J. Cai, J. Lv, Y. Shao, M. H. Rummeli, J. Sun and Z. Liu, *Adv. Mater.*, 2020, **32**, e2003425.

61 P. Sun, L. Ma, W. Zhou, M. Qiu, Z. Wang, D. Chao and W. Mai, *Angew Chem. Int. Ed. Engl.*, 2021, **60**, 18247–18255.
62 R. Li, M. C. Li, Y. Chao, J. Q. Guo, G. Xu, B. R. Li, Z. Y. Liu, C. K. Yang and Y. Yu, *Energy Storage Mater.*, 2022, **46**, 605–612.
63 K. Ouyang, D. Ma, N. Zhao, Y. Wang, M. Yang, H. Mi, L. Sun, C. He and P. Zhang, *Adv. Funct. Mater.*, 2022, **32**(7), 2109749.
64 Y. T. Xu, J. J. Zhu, J. Z. Feng, Y. Wang, X. X. Wu, P. J. Ma, X. Zhang, G. Z. Wang and X. B. Yan, *Energy Storage Mater.*, 2021, **38**, 299–308.
65 J. S. Newman and C. W. Tobias, *J. Electrochem. Soc.*, 1962, **109**, 1183–1191.
66 J. Newman and W. Tiedemann, *AIChE J.*, 2004, **21**, 25–41.
67 P. M. Gomadam, J. W. Weidner, R. A. Dougal and R. E. White, *J. Power Sources*, 2002, **110**, 267–284.
68 J. S. Chen and H. Y. Cheh, *J. Electrochem. Soc.*, 2019, **140**, 1205–1213.
69 J. S. Chen and H. Y. Cheh, *J. Electrochem. Soc.*, 2019, **140**, 1213–1218.
70 E. J. Podlaha and H. Y. Cheh, *J. Electrochem. Soc.*, 2019, **141**, 15–27.
71 T. W. Farrell, C. P. Please, D. L. S. McElwain and D. A. J. Swinkels, *J. Electrochem. Soc.*, 2000, **147**, 4034–4044.
72 Y. Zeng, X. Zhang, R. Qin, X. Liu, P. Fang, D. Zheng, Y. Tong and X. Lu, *Adv. Mater.*, 2019, **31**, e1903675.
73 J. Lee, H. S. Lim, X. Cao, X. Ren, W. J. Kwak, I. A. Rodriguez-Perez, J. G. Zhang, H. Lee and H. T. Kim, *ACS Appl. Mater. Interfaces*, 2020, **12**, 37188–37196.
74 H. L. Qiu, T. Y. Tang, M. Asif, W. Li, T. Zhang and Y. L. Hou, *Nano Energy*, 2019, **65**, 103989.
75 Q. Yang, Y. Guo, B. Yan, C. Wang, Z. Liu, Z. Huang, Y. Wang, Y. Li, H. Li, L. Song, J. Fan and C. Zhi, *Adv. Mater.*, 2020, **32**, e2001755.
76 J. F. Parker, C. N. Chervin, E. S. Nelson, D. R. Rolison and J. W. Long, *Energy Environ. Sci.*, 2014, **7**, 1117–1124.
77 Q. Yang, G. Liang, Y. Guo, Z. Liu, B. Yan, D. Wang, Z. Huang, X. Li, J. Fan and C. Zhi, *Adv. Mater.*, 2019, **31**, e1903778.
78 L. T. Kang, M. W. Cui, F. Y. Jiang, Y. F. Gao, H. J. Luo, J. J. Liu, W. Liang and C. Y. Zhi, *Adv. Energy Mater.*, 2018, **8**, 1801090.
79 Z. M. Zhao, J. W. Zhao, Z. L. Hu, J. D. Li, J. J. Li, Y. J. Zhang, C. Wang and G. L. Cui, *Energy Environ. Sci.*, 2019, **12**, 1938–1949.
80 M. F. Lagadec, R. Zahn and V. Wood, *Nat. Energy*, 2019, **4**, 16–25.
81 M. S. Gonzalez, Q. Yan, J. Holoubek, Z. Wu, H. Zhou, N. Patterson, V. Petrova, H. Liu and P. Liu, *Adv. Mater.*, 2020, **32**, e1906836.
82 J. Q. Huang, W. G. Chong and B. Zhang, *J. Power Sources*, 2024, **594**, 234036.
83 Y. Kubo, Y. Hayashi and M. Ueta, Separator Paper for Alkaline Battery and the Alkaline Battery, *US Pat.*, 0014080, 2006.
84 P. Arora and Z. J. Zhang, *Chem. Rev.*, 2004, **104**, 4419–4462.
85 P. Kritzer and J. A. Cook, *J. Electrochem. Soc.*, 2007, **154**, A481–A494.
86 H. Qin, W. Chen, W. Kuang, N. Hu, X. Zhang, H. Weng, H. Tang, D. Huang, J. Xu and H. He, *Small*, 2023, **19**, e2300130.
87 Y. Liu, S. Liu, X. Xie, Z. Li, P. Wang, B. Lu, S. Liang, Y. Tang and J. Zhou, *InfoMat*, 2022, **5**, e12374.
88 J. Cao, D. D. Zhang, C. Gu, X. Wang, S. M. Wang, X. Y. Zhang, J. Q. Qin and Z. S. Wu, *Adv. Energy Mater.*, 2021, **11**, 2101299.
89 Y. Qin, P. Liu, Q. Zhang, Q. Wang, D. Sun, Y. Tang, Y. Ren and H. Wang, *Small*, 2020, **16**, e2003106.
90 J. Li, Y. Chen, J. Guo, F. Wang, H. Liu and Y. Li, *Adv. Funct. Mater.*, 2020, **30**, 2004115.
91 W. Zhou, M. Chen, Q. Tian, J. Chen, X. Xu and C.-P. Wong, *Energy Storage Mater.*, 2022, **44**, 57–65.
92 T. C. Liu, J. Hong, J. L. Wang, Y. Xu and Y. Wang, *Energy Storage Mater.*, 2022, **45**, 1074–1083.
93 J. Cao, D. D. Zhang, X. Y. Zhang, M. Sawangphruk, J. Q. Qin and R. P. Liu, *J. Mater. Chem. A*, 2020, **8**, 9331–9344.
94 Y. C. Liang, Y. Y. Wang, H. W. Mi, L. N. Sun, D. T. Ma, H. W. Li, C. X. He and P. X. Zhang, *Chem. Eng. J.*, 2021, **425**, 131862.
95 M. Chen, J. Chen, W. Zhou, X. Han, Y. Yao and C. P. Wong, *Adv. Mater.*, 2021, **33**, e2007559.
96 Y. Song, P. Ruan, C. Mao, Y. Chang, L. Wang, L. Dai, P. Zhou, B. Lu, J. Zhou and Z. He, *Nano-Micro Lett.*, 2022, **14**, 218.
97 D. Yang, X. Wu, L. He, Z. Sun, H. Zhao, M. Wang, Y. Wang and Y. Wei, *Nano Lett.*, 2023, **23**, 336–343.
98 J. Zhou, Z. Zhang, W. Jiang, S. J. Hou, K. Yang, Q. Li, L. M. Pan and J. Yang, *J. Alloys Compd.*, 2023, **950**, 169836.
99 G. Lin, X. Zhou, L. Liu, H. Li, D. Huang, J. Liu, J. Li and Z. Wei, *RSC Adv.*, 2023, **13**, 6453–6458.
100 B. H. Wu, P. P. Wang, H. Y. Yang, Y. L. Liang, W. T. Ni, G. B. Xu, X. L. Wei and L. W. Yang, *J. Power Sources*, 2023, **580**, 233323.
101 D. Huang, X. L. Zhou, L. M. Liu, H. M. Li, G. Lin, J. Li and Z. H. Wei, *Colloids Surf., A*, 2023, **663**, 130991.
102 X. Zhang, J. Li, K. Qi, Y. Yang, D. Liu, T. Wang, S. Liang, B. Lu, Y. Zhu and J. Zhou, *Adv. Mater.*, 2022, **34**, e2205175.
103 Y. An, Y. Tian, Q. Man, H. Shen, C. Liu, Y. Qian, S. Xiong, J. Feng and Y. Qian, *ACS Nano*, 2022, **16**, 6755–6770.
104 Z. Wang, L. Dong, W. Huang, H. Jia, Q. Zhao, Y. Wang, B. Fei and F. Pan, *Nano-Micro Lett.*, 2021, **13**, 73.
105 C. Wei, L. Tan, Y. Zhang, S. Xiong and J. Feng, *ChemPhysMater*, 2022, **1**, 252–263.
106 X. Liu, F. Yang, W. Xu, Y. Zeng, J. He and X. Lu, *Adv. Sci.*, 2020, **7**, 2002173.
107 B. Karadeniz, A. J. Howarth, T. Stolar, T. Islamoglu, I. Dejanovic, M. Tireli, M. C. Wasson, S. Y. Moon, O. K. Farha, T. Friscic and K. Uzarevic, *ACS Sustain. Chem. Eng.*, 2018, **6**, 15841–15849.
108 T. J. Zhao, H. Y. Wu, X. H. Wen, J. Zhang, H. B. Tang, Y. J. Deng, S. J. Liao and X. L. Tian, *Coord. Chem. Rev.*, 2022, **468**, 214642.
109 W. L. Xin, J. Xiao, J. W. Li, L. Zhang, H. L. Peng, Z. C. Yan and Z. Q. Zhu, *Energy Storage Mater.*, 2023, **56**, 76–86.

110 Y. Yang, H. M. Hua, Z. H. Lv, W. W. Meng, M. H. Zhang, H. Li, P. X. Lin, J. Yang, G. H. Chen, Y. H. Kang, Z. P. Wen, J. B. Zhao and C. C. Li, *ACS Energy Lett.*, 2023, **8**, 1959–1968.
111 X. M. Liu, F. G. Kong, Z. R. Wang, M. M. Ren, C. D. Qiao, W. L. Liu, J. S. Yao, C. B. Zhang and H. Zhao, *Scr. Mater.*, 2023, **233**, 115520.
112 X. P. Yang, W. L. Wu, Y. Z. Liu, Z. R. Lin and X. Q. Sun, *Chem. Eng. J.*, 2022, **450**, 137902.
113 H. Ma, J. Q. Yu, M. F. Chen, X. Han, J. Z. Chen, B. Liu and S. Q. Shi, *Adv. Funct. Mater.*, 2023, **33**, 2307384.
114 E. Lizundia, C. M. Costa, R. Alves and S. Lanceros-Méndez, *Carbohydr. Polym. Technol. Appl.*, 2020, **1**, 100001.
115 J. Cao, D. D. Zhang, C. Gu, X. Y. Zhang, M. Okhawilai, S. M. Wang, J. T. Han, J. Q. Qin and Y. H. Huang, *Nano Energy*, 2021, **89**, 106322.
116 Y. Yang, T. Chen, B. X. Yu, M. K. Zhu, F. B. Meng, W. Shi, M. C. Zhang, Z. C. Qi, K. Y. Zeng and J. M. Xue, *Chem. Eng. J.*, 2022, **433**, 134077.
117 X. N. Zhang, S. C. Yang, Z. Huang, Z. Zeng, Y. Zhang and Z. H. Wang, *Electrochim. Acta*, 2022, **430**, 141081.
118 X. S. Ge, W. H. Zhang, F. C. Song, B. Xie, J. D. Li, J. Z. Wang, X. J. Wang, J. W. Zhao and G. L. Cui, *Adv. Funct. Mater.*, 2022, **32**, 2200429.
119 Y. Zhang, X. Li, L. S. Fan, Y. Shuai and N. Q. Zhang, *Cell Rep. Phys. Sci.*, 2022, **3**, 100824.
120 P. H. Cao, H. C. Zhou, X. Y. Zhou, Q. Du, J. J. Tang and J. Yang, *ACS Sustainable Chem. Eng.*, 2022, **10**, 8350–8359.
121 H. Zhang, M. Y. Zhou, C. E. Lin and B. K. Zhu, *RSC Adv.*, 2015, **5**, 89848–89860.
122 M. Guo, J. Xiong, X. Y. Jin, S. J. Lu, Y. F. Zhang, J. Xu and H. S. Fan, *J. Membr. Sci.*, 2023, **675**, 121533.
123 F. A. Zakil, S. K. Kamarudin and S. Basri, *Renewable Sustainable Energy Rev.*, 2016, **65**, 841–852.
124 I. Bauer, S. Thieme, J. Brückner, H. Althues and S. Kaskel, *J. Power Sources*, 2014, **251**, 417–422.
125 J. T. Wang, P. F. Zhai, T. K. Zhao, M. J. Li, Z. H. Yang, H. Q. Zhang and J. J. Huang, *Electrochim. Acta*, 2019, **320**, 134558.
126 M. Ghosh, V. Vijayakumar and S. Kurungot, *Energy Technol.*, 2019, **7**, 1900442.
127 B. K. Wu, Y. Z. Wu, Z. D. Lu, J. S. Zhang, N. Han, Y. M. Wang, X. M. Li, M. Lin and L. Zeng, *J. Mater. Chem. A*, 2021, **9**, 4734–4743.
128 M. Ghosh, V. Vijayakumar, B. Anothumakkool and S. Kurungot, *ACS Sustain. Chem. Eng.*, 2020, **8**, 5040–5049.
129 I. V. Kolesnichenko, D. J. Arnot, M. B. Lim, G. G. Yadav, M. Nyce, J. Huang, S. Banerjee and T. N. Lambert, *ACS Appl. Mater. Interfaces*, 2020, **12**, 50406–50417.
130 Y. Fang, X. Xie, B. Zhang, Y. Chai, B. Lu, M. Liu, J. Zhou and S. Liang, *Adv. Funct. Mater.*, 2021, **32**, 2109671.
131 J. L. Hu, Y. D. Qu, F. W. Shi, J. K. Wang, X. He, S. Q. Liao and L. F. Duan, *Adv. Funct. Mater.*, 2022, **32**, 2209463.
132 Y. C. Liang, D. T. Ma, N. Zhao, Y. Y. Wang, M. Yang, J. B. Ruan, G. H. Yang, H. W. Mi, C. X. He and P. X. Zhang, *Adv. Funct. Mater.*, 2022, **32**, 2112936.
133 T. N. Nguyen, B. Iranpour, E. Cheng and J. D. W. Madden, *Adv. Energy Mater.*, 2021, **12**, 2103148.
134 J. C. Huang, G. Yadav, D. E. Turney, J. S. Cho, M. Nyce, B. R. Wygant, T. N. Lambert and S. Banerjee, *ACS Appl. Energy Mater.*, 2022, **5**, 9952–9961.
135 Z. X. Liu, D. H. Wang, Z. J. Tang, G. J. Liang, Q. Yang, H. F. Li, L. T. Ma, F. N. Mo and C. Y. Zhi, *Energy Storage Mater.*, 2019, **23**, 636–645.
136 R. A. Sharma, *J. Electrochem. Soc.*, 2019, **135**, 1875–1882.
137 Y. M. Wang, *J. Electrochem. Soc.*, 2019, **137**, 2800–2803.
138 A. Willfahrt, T. Fischer, S. Sahakalkan, R. Martinez, M. Krebes and E. Steiner, *Flexible Printed Electron.*, 2018, **3**, 045004.
139 X. Wang, S. Zheng, F. Zhou, J. Qin, X. Shi, S. Wang, C. Sun, X. Bao and Z. S. Wu, *Natl. Sci. Rev.*, 2020, **7**, 64–72.

